

Electrical stimulation of retinal ganglion cells with diamond and the development of an all diamond retinal prosthesis

Alex E. Hadjinicolaou^{a,b}, Ronald T. Leung^{c,d}, David J. Garrett^{e,*}, Kumaravelu Ganesan^e, Kate Fox^e, David A.X. Nayagam^{c,d}, Mohit N. Shivdasani^c, Hamish Meffin^{f,h}, Michael R. Ibbotson^{b,g}, Steven Prawer^e, Brendan J. O'Brien^{b,g}

^a Research School of Biology, Australian National University, Acton, ACT 0200, Australia

^b National Vision Research Institute, Australian College of Optometry, Corner of Cardigan & Keppel Streets, Carlton, VIC 3053, Australia

^c The Bionics Institute, 384-388 Albert Street, East Melbourne, Victoria 3002, Australia

^d Department of Pathology, The University of Melbourne, St Vincent's Hospital Melbourne, Fitzroy, Victoria 3065, Australia

^e School of Physics, The University of Melbourne, Victoria 3010, Australia

^f NICTA, Department of Electrical and Electronic Engineering, University of Melbourne, Victoria 301, Australia

^g Dept. of Optometry & Vision Science, University of Melbourne, Corner of Cardigan & Keppel Streets, Carlton, VIC 3053, Australia

^h Department of Electrical and Electronic Engineering, The University of Melbourne, Victoria 3010, Australia

ARTICLE INFO

Article history:

Received 19 April 2012

Accepted 30 April 2012

Available online 20 May 2012

Keywords:

Bionic
Retina
Diamond
Neural stimulation

ABSTRACT

Electronic retinal implants for the blind are already a market reality. A world wide effort is underway to find the technology that offers the best combination of performance and safety for potential patients. Our approach is to construct an epi-retinally targeted device entirely encapsulated in diamond to maximise longevity and biocompatibility. The stimulating array of our device comprises a monolith of electrically insulating diamond with thousands of hermetic, microscale nitrogen doped ultra-nanocrystalline diamond (N-UNCD) feedthroughs. Here we seek to establish whether the conducting diamond feedthroughs of the array can be used as stimulating electrodes without further modification with a more traditional neural stimulation material. Efficacious stimulation of retinal ganglion cells was established using single N-UNCD microelectrodes in contact with perfused, explanted, rat retina. Evoked rat retinal ganglion cell action potentials were recorded by patch clamp recording from single ganglion cells, adjacent to the N-UNCD stimulating electrode. Separately, excellent electrochemical stability of N-UNCD was established by prolonged pulsing in phosphate buffered saline at increasing charge density up to the measured charge injection limit for the material.

© 2012 Elsevier Ltd. All rights reserved.

1. Introduction

The emergence of electronic retinal implants has the potential to significantly improve the lives of people suffering from several diseases that cause blindness [1–3]. The majority of existing implants consist of an array of electrodes that are surgically implanted into a position on or near the damaged retina. Data from the visual field is mapped onto the electrode array and the retina is electrically stimulated accordingly. Currently, three implantation locations for the electrode array dominate, namely; epiretinal (on the inner retina) [4,5], sub-retinal (between the retina and the choroid) [6–8] or suprachoroidal (between the choroid and the

sclera) [9]. A representation of the visual field is typically captured either by a camera worn by the user or by a photodiode array on the retinal device itself. Visual data from a camera can be sent to the retinal implant via either a wired or wireless link (Fig. 1). Photodiode arrays on a retinal implants have the advantage that the diodes can be directly mapped to stimulating electrodes such that the image transduction and stimulating array move with the eye. The disadvantage of photodiode arrays is that they are electronically relatively simple giving the user limited control of stimulation parameters or image manipulation [6]. Alternatively, data fed from a camera source can be relayed to a stimulating array in many different ways potentially making the device useful under a wider variety of conditions and better able to adapt to varying user needs and developments in information technology. The current generation of implants have sufficient resolution to aid the user with basic navigation [5] and in some instances reading of large high

* Corresponding author. Tel.: +61 39035 4973; fax: +61 3 9347 4783.
E-mail address: dgarrett@unimelb.edu.au (D.J. Garrett).

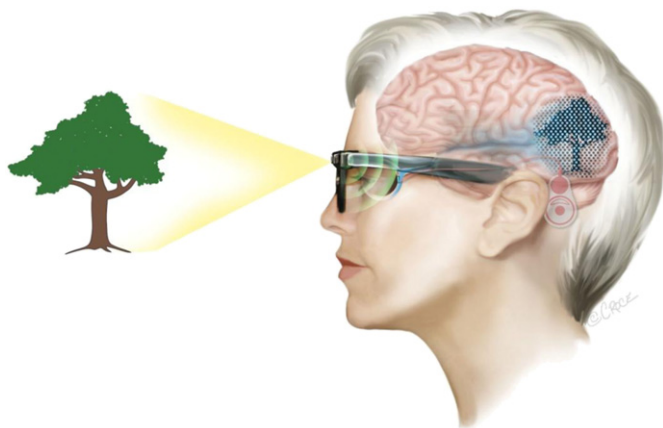


Fig. 1. Illustration depicting image capture of a visual scene by a camera mounted on a pair of glasses. The visual data is relayed via a wireless link to an implanted retinal device that electronically stimulates the retina with a special pattern derived from the image. The stimulation pattern on the retina is relayed to the brain via the optic nerve providing the visual system with sufficient information to generate visual perception.

contrast print [6]. An aim for future devices is to achieve higher resolution and consequently a more useful and naturalistic visual experience for patients.

Materials selection for fabrication of electronic implants is critically important, in particular where the device is exposed to the body. To protect the device's electronics from the body, the device must exhibit excellent hermeticity. To protect the user from the device, it must additionally exhibit biocompatibility and biochemical stability. All materials must be resistant to sterilisation procedures, mechanically robust, and sufficiently biochemically inert to operate continuously, potentially for decades. Diamond is a material that possesses all of these properties.

The chemical and mechanical stability of diamond is well known. The device being developed as part of the Bionic Vision Australia (BVA) initiative is an epiretinal design that will interface with a head-mounted camera. The stimulating array and electronics capsule of this device will be fabricated entirely from diamond. The form of the current generation of the Bionic Vision Australia (BVA) epiretinal device, as shown in Fig. 2(a), incorporates a diamond capsule which houses the stimulator electronics and feedthrough array, soft silicone wings, retinal tack attachments as well as a data and power lead. The device will utilise electrically insulating polycrystalline diamond and electrically conducting N-UNCD, both of which have been shown to exhibit excellent biocompatibility [10,11]. The limited use of diamond in electronic devices can be attributed to the fact that diamond is difficult to shape and manipulate due to its extreme hardness and lack of ductility. We have developed a suite of techniques for manipulating diamond structures including fabrication of capsules, microneedles [12] and high numbers of conducting diamond feedthroughs in monolithic polycrystalline diamond films. A micrograph of our diamond electrode interface array is shown in Fig. 2(b) and (c). The array is constructed from a flat sheet of electrically insulating polycrystalline diamond through which feedthrough holes are cut. The feedthroughs are backfilled with conducting N-UNCD.

Of critical importance to the long term efficacy of an electronic retinal prosthesis is the electrochemical performance of the electrodes that are physically in contact with the retina. The electrodes must be able to deliver enough charge to evoke action potentials from ganglion cells whilst remaining within safe voltage limits [13]. In electrochemical terms this translates to a high electrode capacitance. We have previously shown that N-UNCD can be coated with platinum or electrochemically formed iridium oxide to increase

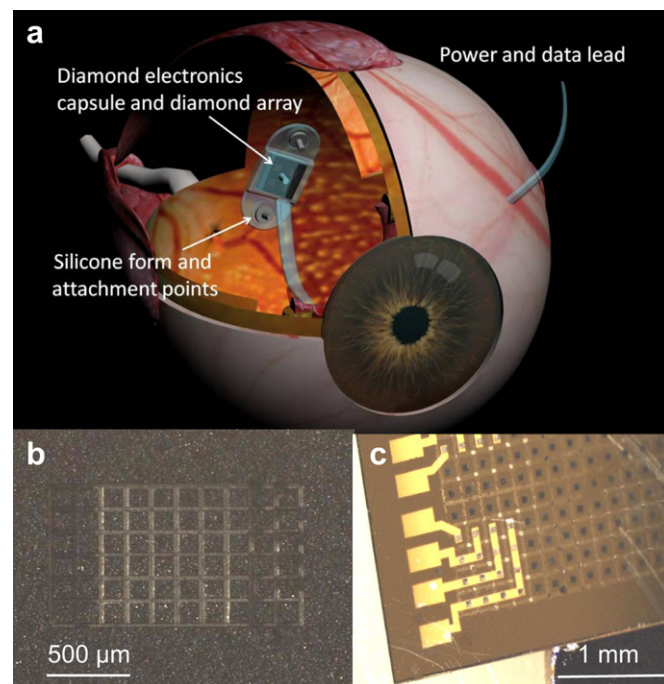


Fig. 2. (a) Medical illustration of the form for the BVA epiretinal device, tacked in position over the macula, (b) Micrograph of the external face of a diamond feedthrough array. The black squares are conducting N-UNCD and the lighter lines are exposed PCD through which light is transmitted. Some light through the array is blocked by evaporated wires on the reverse side. (c) Interior face of the feedthrough array with evaporated metal wires contacting some feedthroughs.

charge injection [14]. Though coating of the N-UNCD feedthroughs with a high charge injection material is an option, it is one that comes with associated risks (e.g. delamination) [15]. It is advantageous both in terms of risk mitigation and fabrication simplicity if the N-UNCD feedthroughs can be used as the stimulating electrodes. We have previously established that by tailoring growth conditions and electrochemical activation the charge injection capacity (Q_c) of N-UNCD can be increased to values where neural stimulation becomes feasible [14]. Here we demonstrate that N-UNCD can effectively stimulate retinal ganglion cells (RGCs) whilst remaining within electrochemical limits. We also show that N-UNCD exhibits very stable electrochemistry over extended use even when operating at the predefined electrochemical limits. Efficacious stimulation of RGCs is demonstrated by direct stimulation of RGCs in explanted rat retina. Responses from individual RGCs were recorded using the patch clamp recording technique. The collated threshold charge values required to affect a ganglion response are compared to the charge injection value established for the N-UNCD electrodes showing that efficacious stimulation was achieved well within the predefined electrochemical limits.

2. Materials and methods

2.1. N-UNCD microelectrode fabrication and characterization

2.1.1. Fabrication

Fifty micrometre (μm) thick films of N-UNCD were grown in an Iplasma microwave plasma assisted chemical vapour deposition (CVD) system. Samples were grown with a gas mixture of 20:79:1 N_2 :Ar: CH_4 under conditions that have been described in detail elsewhere [14]. Single $200 \times 200 \mu\text{m}$ square N-UNCD electrodes were prepared for retinal electrophysiology experiments (Fig. 3(a)). A 0.5 mm wide strip of N-UNCD was brazed to 100 μm thick tantalum foil in a high vacuum thermal annealer using a commercial diamond brazing alloy. Individual electrodes were cut from the brazed diamond/tantalum using a laser cutter (Oxford Lasers). The size of the electrode was reduced to $200 \times 200 \mu\text{m}$ by laser milling of the excess diamond.

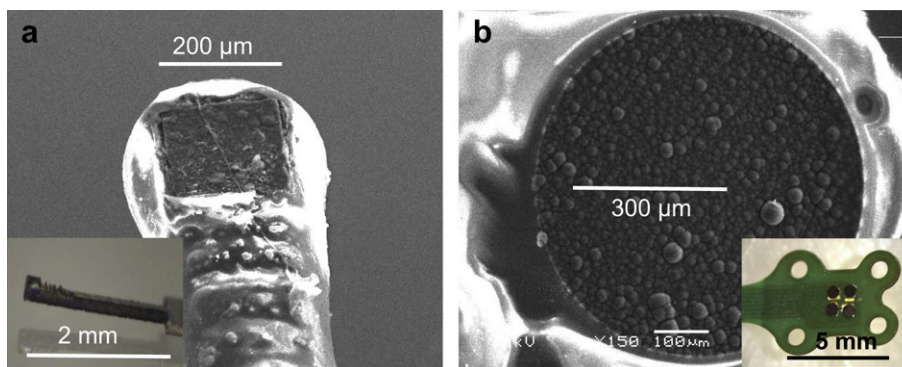


Fig. 3. (a) SEM image of a $200 \times 200 \mu\text{m}$ square N-UNCD electrode that has been used as a stimulating electrode on excised rat retina. Inset is a micrograph of the electrode before insulation with epoxy and silicone. (b) An SEM image of a $600 \mu\text{m}$ diameter N-UNCD disc electrode used to assess electrochemical stability. Inset is a micrograph of four such electrodes attached to a flexible circuit board and isolated with epoxy resin.

The metal shaft was insulated by placing a bead of silicone rubber on the electrode face under a microscope and then hand painting the tantalum shaft and electrode sides with epoxy resin. Finally the silicone rubber bead was removed to reveal only the face of the N-UNCD electrode and a final layer of silicone was applied to the shaft and the sides of the N-UNCD electrode. Electrical connection to the stimulator was made through the tantalum shaft.

Electrode arrays for electrochemical stability studies were four $600 \mu\text{m}$ diameter round discs of N-UNCD, synthesized under the same growth conditions (Fig. 3(b)). The N-UNCD was cut by laser and glued to pads on a custom designed flexible printed circuit board (flexible circuits, USA) using conductive epoxy (Circuitworks, chemtronics, USA). The electrodes were isolated by painting insulating epoxy resin around the electrodes and over the flex circuit under a microscope.

Both types of electrodes were electrochemically activated by three cyclic voltammograms (CVs) from 200 mV to 2.5 V vs. Ag/AgCl at a scan rate of 100 mV s^{-1} in pH 7.4 50 mM phosphate buffer with 0.13 M NaCl (PBS), according to our previously established protocol [14].

2.1.2. Electrochemical characterization

All cyclic voltammetry (CV) and some chronopotentiometry was conducted using an eDAQ EA163 potentiostat and a conventional 3 electrode electrochemical cell arrangement with a 1 M Ag/AgCl reference electrode and a platinum wire counter electrode in PBS.

2.2. Electrochemical stability assessment

Interleaved stimulation of four $600 \mu\text{m}$ diameter N-UNCD disk electrodes was performed with a custom-built stimulator at current levels of $200 \mu\text{A}$, $700 \mu\text{A}$, $1200 \mu\text{A}$ and $1700 \mu\text{A}$ for 7 days such that all electrodes were subjected to a pulse frequency of 50 Hz . The range of current amplitudes was chosen to span the charge injection limit range N-UNCD. Biphasic, cathodic first, charge balanced pulses of $500 \mu\text{s/phase}$ and $25 \mu\text{s}$ interphase duration were used. A platinum wire with capacitive coupling ($10 \mu\text{F}$) served as the counter electrode. All electrodes were short circuited together between pulses. Current and voltage waveforms (vs. Ag/AgCl reference electrode) were recorded daily (PXI-4072, National Instruments, USA). Stimulation was performed in PBS, replenished daily, at room temperature, in a paraffin film (Parafilm M, Pechiney, USA) sealed petri dish. Scanning electron microscopy (SEM) of all electrodes was performed before and after stimulation using a JEOL JSM-5910 microscope.

2.3. Explanted rat retina electrophysiology

2.3.1. Ethical approval

Methods conformed to the policies of the National Health and Medical Research Council of Australia and were approved by the Animal Ethics Committee of the University of Melbourne.

2.3.2. Retinal wholemount preparation

Detailed procedures have been described previously [16]. In brief, data came from 5 pigmented Long Evans rats ranging in age from 5 to 9 months. Animals were anaesthetized with a mixture of Ketamine (100 mg kg^{-1}) and Xylazine (10 mg kg^{-1}) and enucleated. After enucleation, rats were killed with an overdose of Sodium Pentobarbitone (350 mg , intracardiac). Retinal wholemounts were placed, ganglion cell layer up in the recording chamber (Warner Instruments, Hamden, CT USA, RC-26GLP) and perfused ($4\text{--}6 \text{ ml min}^{-1}$) with carbogenated Ames' medium (Sigma–Aldrich, St. Louis, MO) heated to $34 \text{ }^\circ\text{C}$. The chamber was mounted on the stage of an upright microscope (Olympus, BX51WI) equipped with a $40 \times$ water immersion lens and visualized with infrared optics on a monitor with $4 \times$ additional magnification.

2.3.3. Physiological data collection and analysis

To obtain a whole cell recording, we first made a small hole in the inner limiting membrane and optic fibre layer overlying a ganglion cell [16–18]. Recordings were limited to RGCs exposed during this procedure that had smooth surfaces and agranular cytoplasm. The pipette internal solution contained (in mM): K-gluconate 115, KCl 5, EGTA 5, HEPES 10, Na-ATP 2, Na-GTP 0.25; (mOsm = 273, pH adjusted to 7.3 with KOH) including Alexa Hydrasize 488 ($250 \mu\text{M}$) and biocytin (0.5%). Whole cell current clamp recordings from retinal ganglion cells were obtained with standard procedures [19]. Initial pipette resistance ranged between 3 and $7 \text{ M}\Omega$. After obtaining a gigaohm seal and rupturing the cellular membrane, the pipette series resistance was measured and compensated with the bridge balance circuit of the amplifier. Resting potentials were corrected for the change in liquid junction potential that occurs upon break-in and cell dialysis. The liquid junction potential was measured directly as -5 mV [20]. No capacitance compensation was employed.

Membrane potential was amplified (BA-1S, NPI), digitized with 16 bit precision at 20 kHz (USB-6221, National Instruments) and stored in digital form. The data collected were analysed off-line with custom software developed in Labview (National Instruments). Cells were excluded from analysis if they exhibited marked instability of their resting potential or if their action potentials did not overshoot 0 mV . Once a quality recording was established, we measured each cell's response to biphasic (cathodic first) current stimuli of varying amplitude generated by the stimulator (Multi-Channel Systems, Germany) and delivered through a single diamond electrode ($200 \times 200 \mu\text{m}$) placed upon the inner limiting membrane of the retina immediately adjacent to the recorded cell. Contact with the inner limiting membrane was evident when deformation of the surface of the retina could be seen under the microscope. In all cases, pulse duration of $500 \mu\text{s}$ per phase with an interphase gap of $25 \mu\text{s}$ was used. Each stimulus amplitude was repeated 10 times at a frequency of 1 Hz to generate an intensity response function where response was defined as the percentage of stimuli that evoked one or more action potentials. Individual action potential waveforms were extracted from the stimulus artefact by recording a subthreshold stimulus artefact, scaling it to the appropriate current amplitude, and subtracting it from the raw trace. This procedure is quite similar to that used to remove undesired leakage currents in voltage clamp experiments (p/n protocol, in our case p/3). Threshold was calculated as the current amplitude that evoked 50% efficacy using a two parameter logistic function to fit the data. Responses were recorded from a total of 12 RGCs using three identical electrodes such that each electrode was used to record responses from four RGCs.

2.3.4. Immunocytochemistry and morphological identification

Following recordings, the retinal tissue was removed from the chamber, mounted onto filter paper, fixed for $30\text{--}60 \text{ min}$ in phosphate buffered 4% paraformaldehyde, and stored for up to 2 weeks in 0.1 M phosphate buffered saline (PBS; pH 7.4) at $4 \text{ }^\circ\text{C}$. The tissue was subsequently processed to reveal biocytin filled cells by immersion in 0.5% Triton X-100, $20 \mu\text{g/mL}$ streptavidin conjugated to Alexa488 (Invitrogen) in PBS overnight. Tissue was washed thoroughly in PBS, mounted onto Superfrost + slides and coverslipped in 60% glycerol. Cellular morphology was classified after 3D confocal reconstruction (Zeiss PASCAL).

3. Results

3.1. Electrode characterisation and electrochemical stability

Electrodes were characterized by cyclic voltammetry and chronopotentiometry before and after use. CVs were compared before and after activation and, in the case of the stability study, after use, to assess the degree to which the silicone insulation was leaking (i.e.

thus exposing braze alloy) and to ascertain if electrochemical changes were occurring during use. Chronopotentiograms were recorded before and after activation using biphasic 100 μA amplitude constant current pulses of 1 ms per phase to assess the efficacy of the activation. A further set of chronopotentiograms were recorded to establish maximum charge injection values for the electrodes. These chronopotentiograms were recorded during 500 $\mu\text{s}/\text{phase}$ constant current biphasic pulses of increasing current amplitude until the capacitive voltage excursion (the upward sloping section) during the pulse exceeded 1 V during the anodic phase. This was deemed to be a safe voltage as it lies well below the 1.5 V limit where oxidation of water begins to occur (see Figure S2 and our previous work [14]). Representative CVs and 1 ms per phase chronopotentiograms recorded using both of the electrode types used in the work described here are shown in Fig. 4. Fig. 4(a) and (b) shows CVs and chronopotentiograms (respectively) for 600 μm disc electrodes used in electrochemical stability experiments. Fig. 4(c) and (d) show the corresponding plots for a 200 \times 200 μm square N-UNCD electrode used for explanted rat retina experiments.

The CVs were recorded before (grey trace) and after (black trace) electrochemical activation and in the case of the 600 μm diameter electrode after one week of constant stimulation (dashed trace). Chronopotentiograms were recorded before (grey trace) and after (black trace) activation. The plots shown are typical of all the electrodes discussed in this paper with the exception of Electrode 2 used for explanted rat retina. This electrode exhibited a small amount of silver contamination which is highly likely to have occurred during brazing (Figure S1 supplementary) CVs recorded over the voltage range -2 – 2.2 V (Figure S2 Supplementary) exhibit significant oxidation of water above 1.5 V and reduction of water below -1.6 V consistent with our previous findings [14]. After activation the charge injection capacity of the electrodes was

calculated for biphasic constant current pulses, cathodic first and 500 $\mu\text{s}/\text{pulse}$. The charge injection capacity is derived from the current at which the capacitive charging voltage excursion reached 1 V. For the 600 μm diameter electrodes this occurred at a current amplitude of 1700 $\mu\text{A}/\text{phase}$ (shown in Fig. 5, grey trace), which equates to a charge injection capacity (Q_c) of 300 $\mu\text{C cm}^{-2}$ according to the formula $Q_c = (I \times t)/A$ where I = the current amplitude at which the capacitive voltage excursion reached 1 V, t = the current pulse duration and A = the geometric surface area of the electrode in question. The capacitive charging voltage excursion for the three 200 \times 200 μm square electrodes exceeded 1 V at a current of approximately 200 μA , which equates to $Q_c = 250 \mu\text{C cm}^{-2}$. For all subsequent experiments the charge injection limits for both electrode types was treated as an upper limit for testing. In some cases trace signals from residual braze could not be completely eliminated. Trace contamination was evident by the occurrence of a surface confined chemically reversible couple in the CV with a reduction peak at -0.2 V and an oxidation peak at 0.2 V, which we assume to be silver. Electrodes 1 and 3 described in this article exhibited clean CVs consistent with N-UNCD (e.g. Fig. 4(c)) Electrode 2 exhibited trace silver contamination (Figure S1 supplementary) but was used regardless, because the silver contamination was very low and did not adversely affect the electrochemical water window CV (Figure S2 Supplementary). Pulse characterisation for the three 200 \times 200 μm square electrodes is shown in the supplementary material, Figure S3.

3.2. Electrochemical stability

Voltage wave forms were recorded daily for each of the four current amplitudes tested and the slope of the anodic voltage excursion calculated. Fig. 5(a) shows the voltage excursion

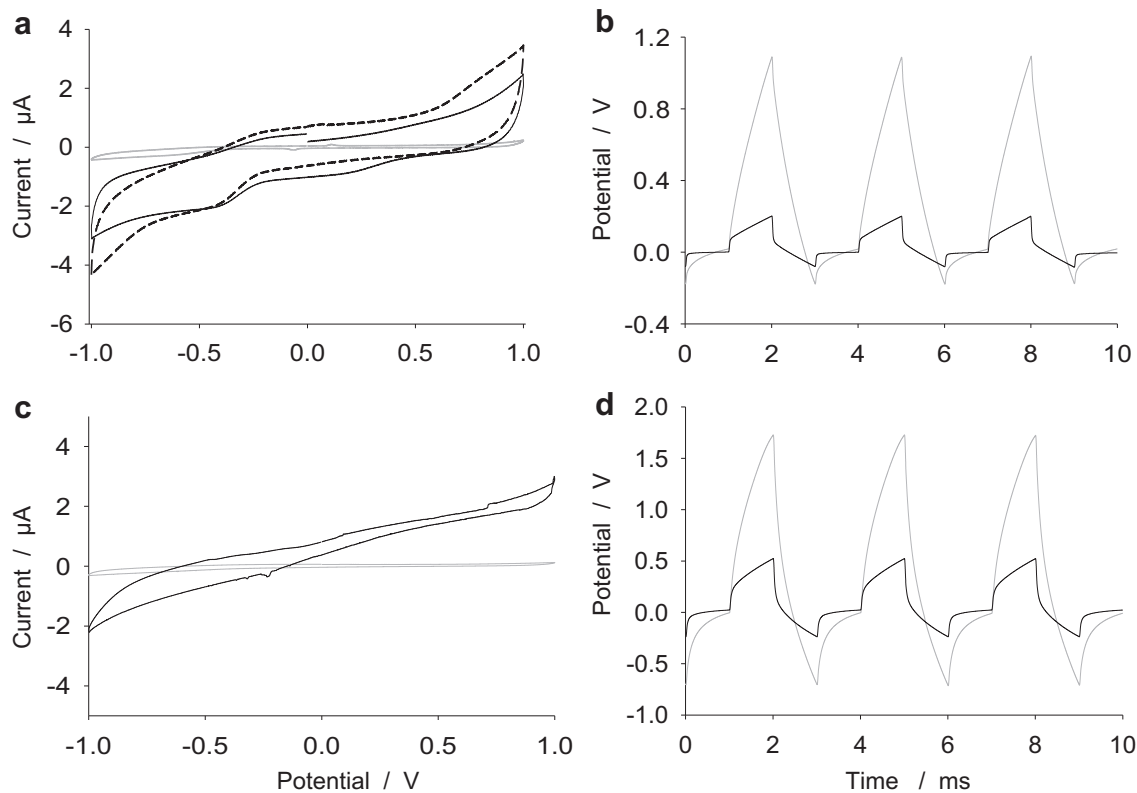


Fig. 4. Representative CVs and voltage traces recorded using the electrode depicted in Fig. 3(b) (plots (a) and (b)) and the electrode depicted in Fig. 3(a) (plots (c) and (d)). CVs were recorded before activation (grey trace), after activation (black trace) and after use (dashed trace). Voltage excursions were recorded during 1 ms, 100 μA per phase, biphasic constant current pulses before (dashed trace) and after (black trace) activation.

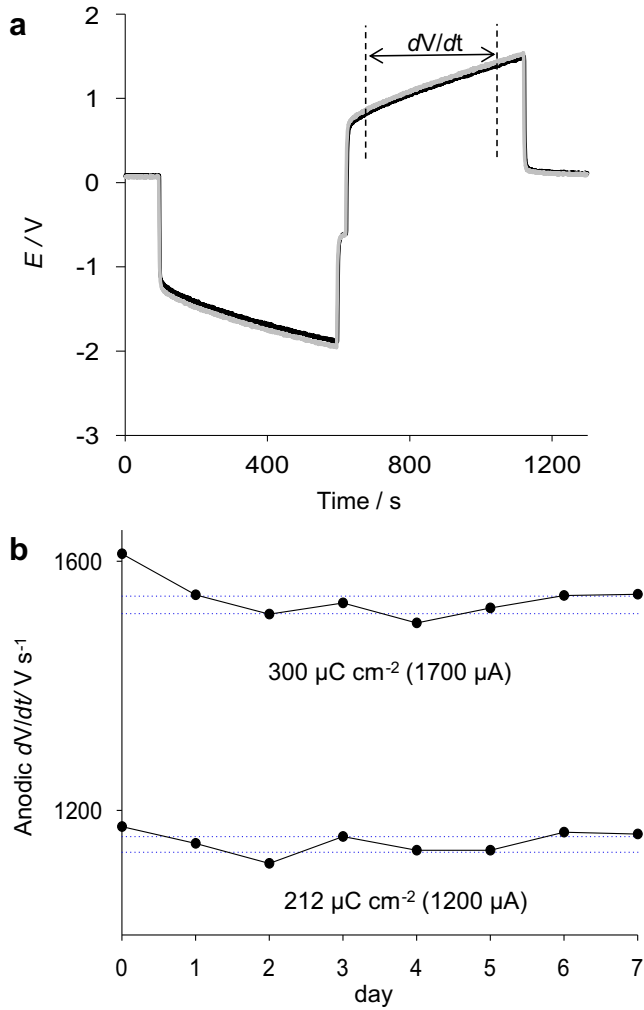


Fig. 5. (a) Representative voltage excursions recorded using a 600 μm diameter N-UNCD electrode during 1700 μA , 500 μs per phase ($300 \mu\text{C cm}^{-2}$), biphasic, constant current pulses, before (grey) and after (black) one week of continuous pulsing at 50 Hz (3×10^7 pulses). Also shown is the region from which daily anodic charging voltage excursion slopes were calculated. (b) Shows day by day anodic excursion slopes recorded during pulsing at the current amplitudes and density indicated on the plots. The dotted lines represent \pm one standard error of the mean or the 95% confidence interval of the mean (day 0 excluded).

occurring during a 1700 μA per phase pulse, before (grey) and after (black) one week of stimulation at 50 Hz. The slope of the voltage excursion during the pulse is related to the electrode capacitance by the relationship $dV/dt = i/C$ where dV/dt is the slope of the voltage excursion (V s^{-1}), i is the pulse current amplitude (A) and C is the electrode capacitance (F) therefore changes in the slope indicate changes in the charge injection capacity. A day by day plot of the slope of the voltage excursion during the anodic phase for the 1700 μA and 1200 μA are shown in Fig. 5(b). The corresponding plots for the 200 μA and 700 μA pulse amplitude electrodes are shown in the supplementary material (Figure S4). Indicated on the plots (dotted lines) are the 95% confidence intervals of the means for the data recorded from days 1–7. In all cases the slope recorded on day 0 lay slightly above the 95% confidence interval and was therefore excluded from calculation of the mean.

3.3. Explanted rat retina electrophysiology

We recorded the physiological responses of 12 rat RGCs to electrical stimulation through 3 different diamond electrodes. Fig. 6

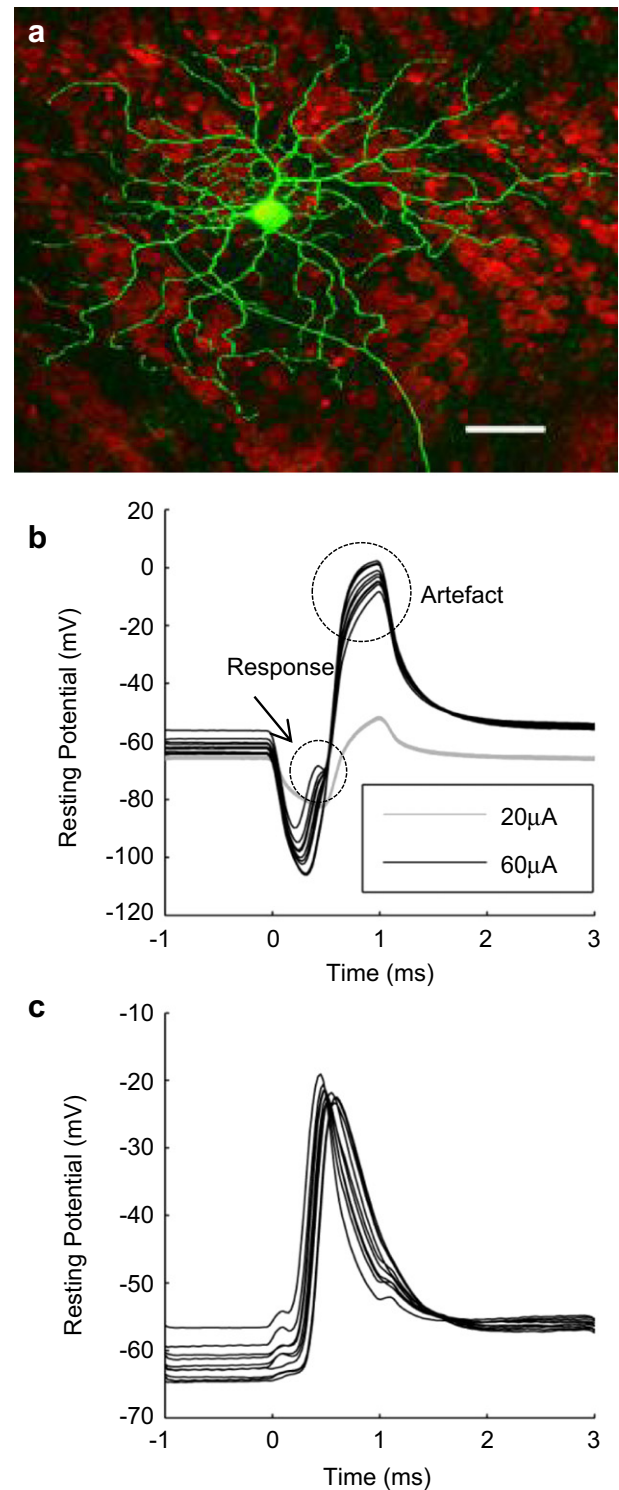


Fig. 6. Rat retinal ganglion cell morphology and response to electrical stimuli. (a) En face view of a confocal reconstruction of the ganglion cell recorded and labelled with Alexa488 (green) along with the propidium iodide labelled cells in the ganglion cell layer (red). Scale bar = 50 μm . (b) Raw responses of the ganglion cell in (a) above to a single subthreshold 20 μA pulse and several responses to 60 μA pulses. (c) Plots of action potentials elicited by the biphasic pulses extracted by scaling of the subthreshold 20 μA response and subtracting it from the 60 μA pulses. (For interpretation of the references to colour in this figure legend, the reader is referred to the web version of this article.)

shows a reconstruction of a typical rat RGC (Fig. 6(a)) which gave rise to the physiological responses shown in Fig. 6(b) and (c). The red stain labels the nuclei of all cells in the ganglion cell layer while the green stain fills the soma, dendrites and axon of the recorded retinal ganglion cell (Fig. 6(a)). Fig. 6(a) shows the cell as it appears in situ in the retina. Based on its morphological features we have identified this as a rat alpha (A2o) ganglion cell [21–23].

The responses of the RGC imaged in Fig. 6(a) to stimulation by the N-UNCD electrode are presented in Fig. 6(b),(c). Electrical stimulation through the N-UNCD electrodes placed upon the surface of the retina adjacent to the recorded cell led to the generation of a stimulus artefact, present in all recordings, and action potentials generated by the recorded ganglion cell. In the raw recordings (Fig. 6(b)) stimuli with low intensity were subthreshold for generating action potentials (e.g. 20 μA trace). These subthreshold traces were scaled appropriately to fit the recorded suprathreshold stimuli (60 μA traces) and subtracted from the raw data to reveal the underlying action potentials (Fig. 6(c)).

Pulse amplitudes were repeated ten times at a frequency of 1 Hz and the individual spikes extracted as described. Efficacy was defined as the percentage of stimuli that elicited an action potential from 10 repeats delivered at 1 Hz (Fig. 7). Each panel in Fig. 7 represents the data obtained from four different cells for the three diamond electrodes we tested. Threshold was defined as 50% efficacy and calculated for each cell by fitting the raw data with a two parameter logistic curve. All curves agreed with the raw data to $r^2 > 0.93$.

4. Discussion

Charging of an electrode surface for neural stimulation should ideally be a non-Faradaic or surface confined Faradaic electrochemical process. Faradaic (electron transfer) processes occurring between an electrode and the biological media or tissue adjacent to the electrode, (e.g. water electrolysis or protein reduction or oxidation) are potentially harmful *in vivo*. The driving force for undesirable Faradaic reactions is the electrical potential (voltage) of the electrode surface. Two electrochemical parameters are critical when assessing the suitability of material for neural stimulation. The first of these is the electrochemical water window which is defined as the voltage range inside which cathodic or anodic water electrolysis does not occur. Our activated N-UNCD electrode consistently exhibits a water window between -1.6 and 1.3 V vs. Ag/AgCl (supplementary material). This is a wider water window than the most commonly used neural stimulation materials (platinum or iridium oxide, -0.6 – 0.8 V vs. Ag/AgCl [13]). Secondly, the electrochemical double layer capacitance or pseudo-capacitance (in the case of electrodes that exhibit surface confined electrochemical reactions, e.g. iridium oxide) must be high. A high capacitance electrode can store a high quantity of charge whilst maintaining a low voltage. Thus, sufficient charge for neural stimulation can be stored at the electrode surface without risking dangerous electrochemical processes occurring. For almost all previously reported forms of diamond, electrochemical capacitance is very low [24,25] making those forms of diamond a desirable material for recording electrodes [26–28], but unsuitable for stimulation. High capacitance forms of diamond are rare and to date are limited to very highly boron doped polycrystalline diamond [29] and N-UNCD [14,30].

As previously observed, we measured a substantial increase in charge injection capacity after electrochemical activation by CV from 200 mV to 2.5 V in PBS. Fig. 4 shows CVs and chronopotentiograms recorded from 600 μm diameter and $200 \times 200 \mu\text{m}$ square N-UNCD electrodes before and after electrochemical activation. Surface capacitance is proportional to the

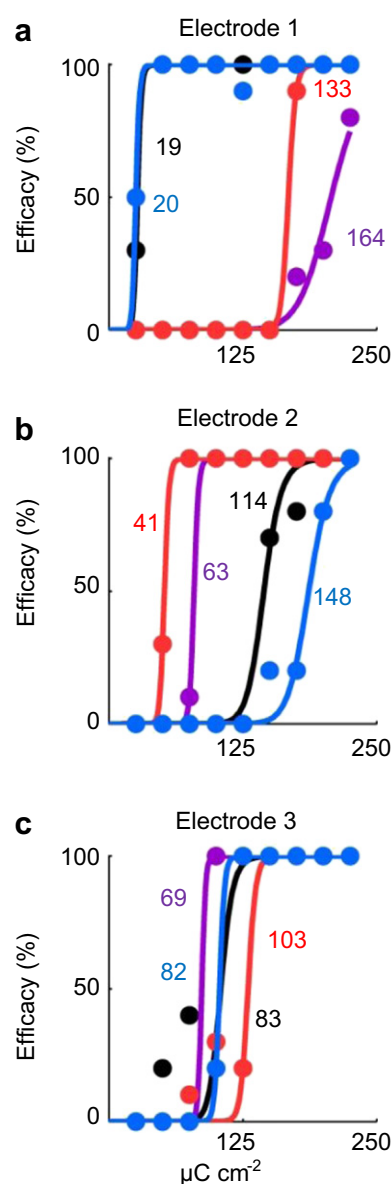


Fig. 7. Intensity response functions of three N-UNCD electrodes. (a) Plots of raw data (coloured points) and their fitted curves (corresponding colours) for four different retinal ganglion cells activated by this electrode. The 50% efficacy threshold current amplitude for each RGC is indicated on each plot. Electrodes were placed in contact with the vitreal surface of the retina and biphasic stimuli of different amplitudes were applied at 1 Hz. Efficacy was defined as the number of stimuli out of 10 that evoked an action potential. Note that all cells reached threshold (50% efficacy) before the charge limitation was reached ($250 \mu\text{C cm}^{-2}$). (b),(c) Intensity response functions obtained using two additional N-UNCD electrodes ($n = 4$ for each). The intensity response function of the cell pictured in Fig. 6 (a) was stimulated with electrode 2, and its response function is the red trace. (For interpretation of the references to colour in this figure legend, the reader is referred to the web version of this article.)

integral area of a CV thus capacitance can be estimated from the anodic and cathodic current magnitude of a CV. The CVs recorded before activation (Fig. 4(a) and (c), grey trace) have very low anodic and cathodic current magnitudes and therefore relatively low double layer capacitance. After activation (black traces in Fig. 4(a) and (c)), the CV current magnitudes increased significantly indicating increased capacitance. There is a discernible Faradaic reduction peak at -0.5 V, which is attributed to dissolved oxygen. Otherwise the CVs are free of any reversible peaks associated with surface confined chemically reversible Faradaic reactions, consistent with diamond electrochemistry and indicate charging via

electrochemical double layer capacitance. The voltage traces depicted in Fig. 4(b) and (d) show the effect of activation on the electrode voltage excursion during a 100 μA amplitude, constant current, biphasic, 1 ms/phase neural stimulation pulse. The voltage required to drive the pulse before activation (dashed trace) is large in contrast to the activated electrode (black trace) where the voltage required is significantly lower. By pulsing the electrode at currents of increasing magnitude it is possible to define a maximum current amplitude for a given pulse condition by defining a voltage limit (1 V) that the electrode surface must not exceed. It is important to note that the voltage at the electrode surface is represented by the voltage magnitude over which the electrode rises after the initial rapid voltage change as the pulse is applied. This initial sharp voltage change (access voltage) is required to overcome the electrode solution interface impedance and any other resistances in the circuit (according to Ohm's law) and thus is not actually present on the electrode surface. The maximum currents at which the capacitive voltage excursions exceed 1 V for 500 μs per phase pulses were approximately 1700 μA for the 600 μm diameter electrodes and 200 μA for the $200 \times 200 \mu\text{m}$ square electrodes which equates to a charge injection capacity of 300 $\mu\text{C cm}^{-2}$ and 250 $\mu\text{C cm}^{-2}$, respectively. It is unclear why the two types of electrodes exhibited different charge injection values. The N-UNCD sheets used to make the electrodes came from different growth runs and thus may indicate an area where a higher degree of process control is required. These values of 300 and 250 $\mu\text{C cm}^{-2}$ are significantly higher than our previously reported value of 163 $\mu\text{C cm}^{-2}$ recorded using 3 mm diameter N-UNCD electrodes [14]. In that work the charge injection capacities were estimated by observation of the slope of the voltage waveforms at moderate current amplitudes in contrast to the empirical method used here. This illustrates that calculated charge injection values from low amplitude current pulses is not a good predictor of charge injection limits and is a flaw in our previous method. The N-UNCD charge injection values of 250–300 $\mu\text{C cm}^{-2}$ measured here are slightly higher than typical platinum values ($\approx 150 \mu\text{C cm}^{-2}$ [13]) but up to an order of magnitude lower than values reported for IrOx (1000–5000 $\mu\text{C cm}^{-2}$ [13]).

Calculation of the voltage slope during the anodic phase during pulsing revealed a small but significant drop in charge injection capacity between day 0 and day 1 of continuous pulsing (average 4%). Between 1 and 7 days of continuous pulsing the majority of slope values remained within the 95% confidence interval of the mean indicating no further significant change. This may represent a clear advantage over other materials. Platinum is known to pit and erode with extended use even when used well inside electrochemical limits [31,32] and some forms of iridium oxide have been shown degrade and/or delaminate in particular when the cathodic voltage excursion exceeds -0.6 V [15,33]. In all cases the voltage slopes are close to constant during the majority of the pulse indicating that no Faradaic (water electrolysis) processes are occurring. We observed no discernable changes in the surface morphology of the electrodes under SEM after the week of continuous pulsing. Little or no morphological or electrochemical change during prolonged use is an important electrode property because degradation of electrode material over long duty cycles is a potential limiter of device lifetime. Changes in the morphology or electrochemistry over time also represent risk factors because electrode voltages may stray to values that are unsafe *in vivo*. The after use CV shown in Fig. 4(b) (dashed trace) was recorded after a three week delay and after a reactivation cycle of 3 CVs from 200 mV to 2.5 V vs. Ag/AgCl. The CV is very similar to the freshly activated CV indicating very little electrochemical change over the week long stimulation period. A reactivation cycle was required as the charge injection capacity of the electrodes reduced by between 20 and 30% over the

three weeks of storage in air. Previously we established by XPS analysis that the strongest predictor of high charge injection capacity in N-UNCD was oxygen concentration in the material and we also showed that electrochemical activation increased oxygen concentration [14]. Oxygen functionalization could increase capacitance by specific interactions with the electrolyte [29]. In other work, oxygen functionalization of carbon nanotubes led to a 3.2 fold increase in electrochemical double layer capacitance [34] attributed by the authors primarily to an increase in hydrophilicity and electrolyte proton interactions with oxygen functionalities. The loss of charge injection capacity with storage in air is most likely due to adventitious adsorption of carbon species from the air which are readily removed during CV.

Having demonstrated the stability and charge injection capacity of the N-UNCD electrodes we further sought to establish their utility in activating the ganglion cells of the mammalian retina. When placed epi-retinally, close to the somas of the RGCs, the N-UNCD electrodes performed well, activating these cells well below the charge injection limit of 200 $\mu\text{A}/500 \mu\text{s}$ phase (250 $\mu\text{C cm}^{-2}$). This was true for all recorded RGCs. While the average activation curve for each electrode we tested was quite similar, there was a high degree of variability within the pool of cells recorded by each electrode (Fig. 7). This variability in the activation curves may be due to variability in the excitability of different RGC types. It is well established that there are at least 16 different morphological types of RGC in the rat retina [21,22]. Each type is defined by different cellular morphology (size, pattern of dendrites, axon diameter) and is also well known to respond differently to current injection. The variability is well established for both intra and extra-cellular stimulation [16,35,36]. Threshold values could also be affected by the position of the recorded RGC relative to stimulating electrode. Uneven tissue on the retina surfaces means some cells may have been further away from the electrode than others. In this work the RGC response latency of approximately 0.6 ms was consistently observed (e.g. Fig. 6(c)), which is similar to latencies previously reported by Cai et al. [37] and Sekirnjak et al. [35]. Longer spike latencies of approximately 2 ms were observed by Tsai et al. after stimulation from a sub-retinal position [36].

What is clear from our data is that the diamond electrodes are capable of activating the retinal tissue well within the 200 μA current amplitude limitation ($Q_c = 250 \mu\text{C cm}^{-2}$). The lowest thresholds of 19–20 μA were observed with two ganglion cells stimulated using electrode 1 (Fig. 7, Electrode 1, blue and black traces). This equates to a charge injection of 25 $\mu\text{C cm}^{-2}$, well below the limit of 250 $\mu\text{C cm}^{-2}$ established for the electrode. The highest threshold value of 164 μA was also recorded using electrode 1 (Fig. 7, Electrode 1, purple trace) and equates to a charge injection value of 205 $\mu\text{C cm}^{-2}$ which is 82% of the 250 $\mu\text{C cm}^{-2}$ limit. Voltage excursions were not recorded during stimulation owing to equipment limitations but it is reasonable to assume that a voltage of approximately 0.82 V may have been present on the stimulating electrode being 82% of the 1 V limit. Thresholds of 41–133 μA (51–166 $\mu\text{C cm}^{-2}$) were recorded over the 10 remaining cells, again well inside electrochemical limits. Effective stimulation using voltages lower than 1 V is desirable as, though the defined safe voltage of 1 V is well below the water electrolysis limit, it is unknown what other bioelectrochemistry may be occurring in the 0.6–1 V range. It is difficult to compare our threshold results to other wholemount retinal recordings because our electrodes are very large in comparison to most other studies. The $200 \times 200 \mu\text{m}$ electrode size was intentionally chosen because it matches the size of the electrodes on the BVA epiretinal device. Tsai et al. report lowest charge density thresholds of 1430 $\mu\text{C cm}^{-2}$ after subretinal stimulation of wholemount rabbit retina using

a 25 μm diameter Pt-Ir electrode [36]. Sekirnjak et al. consistently measured thresholds less than $10 \mu\text{C cm}^{-2}$ using a 14 μm diameter platinum disc array [35]. Though an isolated RGC response does not necessarily lead to a cortical response, it appears that there is no firm evidence for cortical response thresholds being consistently higher than RGC thresholds. The review of Sekirnjak et al. covers RGC and cortical thresholds and cites reported values over a wide range between 10 and $1200 \mu\text{C cm}^{-2}$. The collated results do not indicate that recording in RGCs or in cortex results in higher thresholds for one technique over the other [35]. The range of threshold results is so broad however that firm conclusions cannot be drawn. DeBalthasar et al. report perceptual thresholds between 5 and $750 \mu\text{C cm}^{-2}$ over 6 human patients fitted with the Argus I device. The Argus I had 16, 260 or 500 μm diameter platinum disc electrodes and was attached in an epiretinal position [38]. In that work they correlate low thresholds with close proximity to the retina.

SEM investigation of the used $200 \times 200 \mu\text{m}$ square electrodes showed limited delamination of the silicone insulation, in particular where it contacted the sides of the diamond electrodes (Fig. 3(a)). It is possible that this may have acted as a source of current leakage by increasing the area of diamond exposed to solution. Furthermore, in this case, some N-UNCD would not have been directly in contact with the retina resulting in a low impedance pathway for current leakage. Current leakage would result in higher threshold values due to loss of some charge into the solution rather than through the tissue, causing the measured threshold to be inflated. Despite this potential current loss our threshold values ($25\text{--}188 \mu\text{C cm}^{-2}$) are at the low end of the spectrum reported by Sekirnjak et al. and are well inside the safe electrochemical limits of the material ($250 \mu\text{C cm}^{-2}$). Thus the results indicate that N-UNCD is electrochemically viable as a material for use as stimulating electrodes for retinal prostheses.

5. Conclusions

N-UNCD electrodes were fabricated and electrochemically activated yielding charge injection values over the range of $250\text{--}300 \mu\text{C cm}^{-2}$. The electrodes exhibited no significant morphological or electrochemical changes after continuous pulsing at the charge injection limit in PBS for one week. N-UNCD electrodes were used to electrically stimulate excised wholemount rat retina eliciting 50% efficacy activation thresholds between 25 and $188 \mu\text{C cm}^{-2}$ for RGCs adjacent to the N-UNCD electrode. Despite the possibility of some current leakage these threshold values are low in the context of existing literature and are well below the safe charge injection limit of $250 \mu\text{C cm}^{-2}$ for N-UNCD. This is a strong indication that N-UNCD is an electrochemically viable material for retinal stimulation. Combined with the high electrochemical stability exhibited, N-UNCD is a promising electrode material for electronic implantable prosthesis applications generally.

Acknowledgements

NICTA is funded by the Australian Government as represented by the Department of Broadband, Communications and the Digital Economy and the Australian Research Council through the ICT Centre of Excellence program. The Bionics Institute acknowledges the support they receive from the Victorian Government through its Operational Infrastructure Program. The authors wish to thank Dr Lois Robblee for her advice and consult. This research was supported by the National Health and Medical Research Council (NHMRC, Project Grant 585440) and the Australian Research Council (ARC) through its Special Research

Initiative (SRI) in Bionic Vision Science and Technology grant to Bionic Vision Australia (BVA).

Appendix A. Supplementary material

Supplementary material associated with this article can be found, in the online version, at doi:10.1016/j.biomaterials.2012.04.063.

References

- [1] SecondSight. Argus II system overview. <http://2-sight.eu/en/system-overview-en>.
- [2] Dowling J. Artificial human vision. *Expert Rev Med Devices* 2005;2:73–85.
- [3] Weiland JD, Cho AK, Humayun MS. Retinal Prostheses: current clinical results and future needs. *Ophthalmology* 2011;118:2227–37.
- [4] Klauke S, Goertz M, Rein S, Hoehl D, Thomas U, Eckhorn R, et al. Stimulation with a wireless intraocular epiretinal implant elicits visual percepts in blind humans. *Invest Ophthalmol Vis Sci* 2011;52:449–55.
- [5] Yanai D, Weiland JD, Mahadevappa M, Greenberg RJ, Fine I, Humayun MS. Visual performance using a retinal prosthesis in three subjects with retinitis pigmentosa. *Am J Ophthalmol* 2007;143:820–7.
- [6] Zrenner E, Wilke R, Bartz-Schmidt KU, Gekeler F, Besch D, Benav H, et al. Subretinal microelectrode arrays allow blind retinitis pigmentosa patients to recognize letters and combine them to words. In: *Proceedings of the 2009 2nd conference on biomedical engineering and informatics*. New York: IEEE; 2009. p. 1049–52.
- [7] Yang YT, Lin PK, Wan C, Yang WC, Lin LJ, Wu CY, et al. Responses of rabbit retinal ganglion cells to subretinal electrical stimulation using a silicon-based microphotodiode array. *Invest Ophthalmol Vis Sci* 2011;52:9353–61.
- [8] Kelly SK, Shire DB, Chen JH, Doyle P, Gingerich MD, Cogan SF, et al. A hermetic wireless subretinal neurostimulator for vision prostheses. *IEEE Trans Biomed Eng* 2011;58:3197–205.
- [9] Shivdasani MN, Luu CD, Cicione R, Fallon JB, Allen PJ, Leuenberger J, et al. Evaluation of stimulus parameters and electrode geometry for an effective suprachoroidal retinal prosthesis. *J Neural Eng* 2010;7:036008.
- [10] Tang L, Tsai C, Gerberich WW, Kruckeberg L, Kania DR. Biocompatibility of chemical-vapor-deposited diamond. *Biomaterials* 1995;16:483–8.
- [11] Aspenberg P, Anttila A, Kontinen YT, Lappalainen R, Goodman SB, Nordsetten L, et al. Benign response to particles of diamond and SiC: bone chamber studies of new joint replacement coating materials in rabbits. *Biomaterials* 1996;17:807–12.
- [12] Ganesan K, Stacey A, Meffin H, Lichter S, Greferath U, Fletcher EL, et al. In: 2010 annual international conference of the IEEE engineering in medicine and biology society. New York: IEEE; 2010. p. 6757–60.
- [13] Cogan SF. Neural stimulation and recording electrodes. *Annu Rev Biomed Eng* 2008;10:275–309.
- [14] Garrett DJ, Ganesan K, Stacey A, Fox K, Meffin H, Prawer S. Ultra-nanocrystalline diamond electrodes: optimization towards neural stimulation applications. *J Neural Eng* 2011;9:016002.
- [15] Cogan SF, Guzelian AA, Agnew WF, Yuen TGH, McCreery DB. Over-pulsing degrades activated iridium oxide films used for intracortical neural stimulation. *J Neurosci Methods* 2004;137:141–50.
- [16] O'Brien BJ, Isayama T, Richardson R, Berson DM. Intrinsic physiological properties of cat retinal ganglion cells. *J Physiol-London* 2002;538:787–802.
- [17] Taylor WR, Wässle H. Receptive field properties of starburst cholinergic amacrine cells in the rabbit retina. *Eur J Neurosci* 1995;7:2308–21.
- [18] Robinson DW, Chalupa LM. The intrinsic temporal properties of alpha and beta retinal ganglion cells are equivalent. *Curr Biol* 1997;7:366–74.
- [19] Hamill OP, Marty A, Neher E, Sakmann B, Sigworth FJ. Improved patch-clamp techniques for high-resolution current recording from cells and cell-free membrane patches. *Pflugers Arch* 1981;391:85–100.
- [20] Neher E. Correction for liquid junction potentials in patch clamp experiments. *Method Enzymol* 1992;207:123–31.
- [21] Huxlin KR, Goodchild AK. Retinal ganglion cells in the albino rat: Revised morphological classification. *J Comp Neurol* 1997;385:309–23.
- [22] Sun WZ, Li N, He SG. Large-scale morphological survey of rat retinal ganglion cells. *Vis Neurosci* 2002;19:483–93.
- [23] Peichl L. Alpha-ganglion and delta-ganglion cells in the rat retina. *J Comp Neurol* 1989;286:120–39.
- [24] Xie ST, Shafer G, Wilson CG, Martin HB. In vitro adenosine detection with a diamond-based sensor. *Diamond Relat Mater* 2006;15:225–8.
- [25] Garrido JA, Nowy S, Hartl A, Stutzmann M. The diamond/aqueous electrolyte interface: an impedance investigation. *Langmuir* 2008;24:3897–904.
- [26] Yoshimi K, Naya Y, Mitani N, Kato T, Inoue M, Natori S, et al. Phasic reward responses in the monkey striatum as detected by voltammetry with diamond microelectrodes. *Neurosci Res* 2011;71:49–62.
- [27] Varney MW, Aslam DM, Janoudi A, Ho-Yin C, Wang DH. Polycrystalline-diamond MEMS biosensors including neural microelectrode-arrays. *Biosensors* 2011;1:118–33.

- [28] Suzuki A, Ivandini TA, Yoshimi K, Fujishima A, Oyama G, Nakazato T, et al. Fabrication, characterization, and application of boron-doped diamond microelectrodes for in vivo dopamine detection. *Anal Chem* 2007;79:8608–15.
- [29] Watanabe T, Shimizu TK, Tateyama Y, Kim Y, Kawai M, Einaga Y. Giant electric double-layer capacitance of heavily boron-doped diamond electrode. *Diamond Relat Mater* 2010;19:772–7.
- [30] Bergonzo P, Bongrain A, Scorsone E, Bendali A, Rousseau L, Lissorgues G, et al. 3D shaped mechanically flexible diamond micro-electrode arrays for eye implant applications: the MEDINAS project. *IRBM* 2011;32:91–4.
- [31] Shepherd RK, Murray MT, Houghton ME, Clark GM. Scanning electron-microscopy of chronically stimulated platinum intracochlear electrodes. *Biomaterials* 1985;6:237–42.
- [32] McHardy J, Robblee LS, Marston JM, Brummer SB. Electrical-stimulation with pt electrodes. 4. factors influencing pt dissolution in inorganic saline. *Biomaterials* 1980;1:129–34.
- [33] Negi S, Bhandari R, Rieth L, Van Wagenen R, Solzbacher F. Neural electrode degradation from continuous electrical stimulation: comparison of sputtered and activated iridium oxide. *J Neurosci Methods* 2010;186:8–17.
- [34] Kim YT, Ito Y, Tadai K, Mitani T, Kim US, Kim HS, et al. Drastic change of electric double layer capacitance by surface functionalization of carbon nanotubes. *Appl Phys Lett* 2005;87:234106.
- [35] Sekirnjak C, Hottowy P, Sher A, Dabrowski W, Litke AM, Chichilnisky EJ. Electrical stimulation of mammalian retinal ganglion cells with multielectrode arrays. *J Neurophysiol* 2006;95:3311–27.
- [36] Tsai D, Morley JW, Suanning GJ, Lovell NH. Direct activation and temporal response properties of rabbit retinal ganglion cells following subretinal stimulation. *J Neurophysiol* 2009;102:2982–93.
- [37] Cai CS, Ren QS, Desai NJ, Rizzo JF, Fried SI. Response variability to high rates of electric stimulation in retinal ganglion cells. *J Neurophysiol* 2011;106:153–62.
- [38] de Balthasar C, Patel S, Roy A, Freda R, Greenwald S, Horsager A, et al. Factors affecting perceptual thresholds in epiretinal prostheses. *Invest Ophthalmol Vis Sci* 2008;49:2303–14.